Int J CARS (2013) 8:335–351
DOI 10.1007/s11548-012-0787-1

ORIGINAL ARTICLE

4D statistical shape modeling of the left ventricle in cardiac MR images

Shahrooz Faghih Roohi · Reza Aghaeizadeh Zoroofi

Received: 31 January 2012 / Accepted: 16 July 2012 / Published online: 15 August 2012

Abstract
Purpose Statistical shape models have shown improved reliability and consistency in cardiac image segmentation. They incorporate a sufficient amount of a priori knowledge from the training datasets and solve some major problems such as noise and image artifacts or partial volume effect. In this paper, we construct a 4D statistical model of the left ventricle using human cardiac short-axis MR images.
Methods Kernel PCA is utilized to explore the nonlinear variation of a population. The distribution of the landmarks is divided into the inter- and intra-subject subspaces. We compare the result of Kernel PCA with linear PCA and ICA for each of these subspaces. The initial atlas in natural coordinate system is built for the end-diastolic frame. The landmarks extracted from it are propagated to all frames of all datasets. We apply the 4D KPCA-based ASM for segmentation of all phases of a cardiac cycle and compare it with the conventional ASM.
Results The proposed statistical model is evaluated by calculating the compactness capacity, specificity and generalization ability measures. We investigate the behavior of the nonlinear model for different values of the kernel parameter. The results show that the model built by KPCA is less compact than PCA but more compact than ICA. Although for a constant number of modes the reconstruction error is a little higher for the KPCA-based statistical model, it produces a statistical model with substantially better specificity than PCA- and ICA-based models.
Conclusion Quantitative analysis of the results demonstrates that our method improves the segmentation accuracy.

S. Faghih Roohi (✉) · R. Aghaeizadeh Zoroofi
University of Tehran, Tehran, Iran
e-mail: shahrooz.roohi@ut.ac.ir

Keywords Cardiac models · 4D statistical shape models · Kernel PCA · Cardiac segmentation

Introduction

Cardiovascular diseases (CVD) are the leading cause of death in the developed world in 2010 [1]. In order to reduce increased rate of mortality and morbidity, early diagnosis and treatment will be inevitable. To accomplish this, currently modern imaging modalities such as MRI allows extracting invaluable information about the anatomy and the function of the heart. Physicians exploit the 4D images of the heart to diagnose the diseases by extracting some clinically precious indices such as ejection fraction (EF), left ventricle volume and mass [2]. These parameters are obtained by segmenting the left ventricle at specific phases of a cardiac cycle. The manual segmentation of the 4D cardiac dataset is a tedious task, so various fully and semi-automated methods were proposed including image-based methods [3], pixel classification [4], biomechanical model [5], deformable models [6], atlas-guided segmentation [7] or statistical shape models. In recent years, statistical shape models have been utilized as strong priori knowledge for some segmentation methods such as active shape model (ASM), active appearance model (AAM) or their combination [8].

Heimann and Meinzer [9] described the various statistical models and their biomedical application. They focused on the point distribution model (PDM) that is a landmark-based method. There were also some alternatives to these models that also enable 3D statistically constrained segmentation such as statistical deformation models [10], probabilistic atlases [11] and a multi-scale 3D shape modeling approach called M-reps [12].

The most popular approach for statistical modeling, which was proposed by Cootes et al. [13], is point distribution model. PDM yields a mean model and its variation modes based on some training datasets. After exploring corresponding landmarks in all datasets, they should be aligned into a common reference coordinate system. The next step is to reduce the dimensionality of the training set and find small modes that describe the variation. Most typical method for this purpose was principal component analysis (PCA).

Some authors applied PCA to build the statistical model for various cardiac chambers of 3D datasets. These models were utilized for various applications such as segmentation or classification. Frangi et al. [14] planned a method for the construction of a 3D statistical shape model of the heart. They modeled the anatomy of the left and right ventricle from 3D MRI datasets. Their work was chosen as a basic framework in significant amount of research. Lotjonen et al. [15] constructed a 3D statistical shape model of atria and ventricles using short- and long-axis cardiac MR images at the end-diastolic phase of a cardiac cycle. Ordas et al. [16] presented a statistical shape model of the whole heart from CT images. The major drawback of use of PCA for dimension reduction was that only the linear variation of landmarks was modeled.

There were not too many works on 4D datasets due to the difference of the temporal and spatial dimensions and huge amount of the data. The method by Perperidis et al. [17] used a 4D transformation model that was separated into decoupled spatial and temporal components. They applied PCA to find the estimate of two subspaces of the overall distribution. They could find what changes in the cardiac anatomy occurred due to the cardiac cycle and what changes occurred due to inter-subject variation. Stegmann and Pedersen [18] presented a framework to estimate the ejection fraction parameter of the left ventricle (LV) in 4D MRI. Zhang et al. [19] built a 4D statistical model to segment the left and right ventricles of normal and tetralogy of fallot (TOF) hearts using PCA. Zhu et al. [20] developed a subject-specific dynamical model (SSDM) that simultaneously handles temporal dynamics (intra-subject variability) and inter-subject variability. Obrien et al. [21] used a PCA-based PDM for statistical shape modeling of the LV. They divided shape, spatial and temporal variation into separate models.

In general, PCA assumes a number of limitations on the data that do not always hold [15,22,23]. Some of these restrictions are as follows:

1. It shows the linear variation of training samples.
2. It finds the directions in which the variance of data is high.
3. It presumes that the cloud of landmark vectors follows a multidimensional Gaussian distribution that is not always true especially for 4D statistical shape modeling.
4. PCA results in global modes that affect all variables simultaneously.

Alternatively, the variation of the training samples was modeled by some other methods such as independent component analysis (ICA). Uzumcu et al. applied ICA to the left and right ventricles in 2D cardiac images. They investigated four methods for sorting the ICA modes [24]. Lotjonen et al. [15] did not sort the ICA modes but selected the few modes of variation that mainly describe the deformations of the atria. Suinesiaputra et al. [22] constructed a classification algorithm from the ICA components to automatically detect and localize abnormally contracting regions of the myocardium. In the other works, it was found that the combination of PCA and ICA improves the segmentation accuracy [25]. ICA and some other methods such as maximum autocorrelation factor (MAF) [26] and minimum noise fraction (MNF) [27] affected the landmarks locally. In these methods, the natural ordering of the variation modes was not straightforward.

There were also some works on constructing statistical models using non-linear PCA. Twining and Taylor [23] suggested kernel PCA (KPCA) to find the variability of the training samples. Several authors applied KPCA for statistical shape analysis of 2D images [28–30], but no one utilized this method for building 3D statistical shape model (SSM) in cardiac dataset.

KPCA does not require a Gaussian distribution of the input data and is able to describe nonlinear shape variations and sort the variation modes. Additionally, there is an increasing interest in using KPCA for implicit shape analysis [9]. To our knowledge, no one utilized this method for building 4D SSM in cardiac dataset.

In this paper, we present a 4D non-linear statistical shape model using KPCA. It models the inner and outer wall of the left ventricle using 4D MR images. This paper makes the following contributions:

1. A novel 4D statistical shape model of the heart LV is proposed. The temporal and spatial variations of the landmarks are separated into two distinct distributions, each is modeled by KPCA.
2. An algorithm is proposed to extract the correspondent landmarks of 4D datasets.
3. A new formula is suggested for the temporal distribution of landmarks.
4. The 4D KPCA-based active shape model is constructed and applied for the LV segmentation at all phases of a cardiac cycle.

In the following, we present a detailed description of our algorithms in the methods section. To investigate the statistical behavior of the proposed model, we compare it with the PCA- and ICA-based models using specificity, compactness

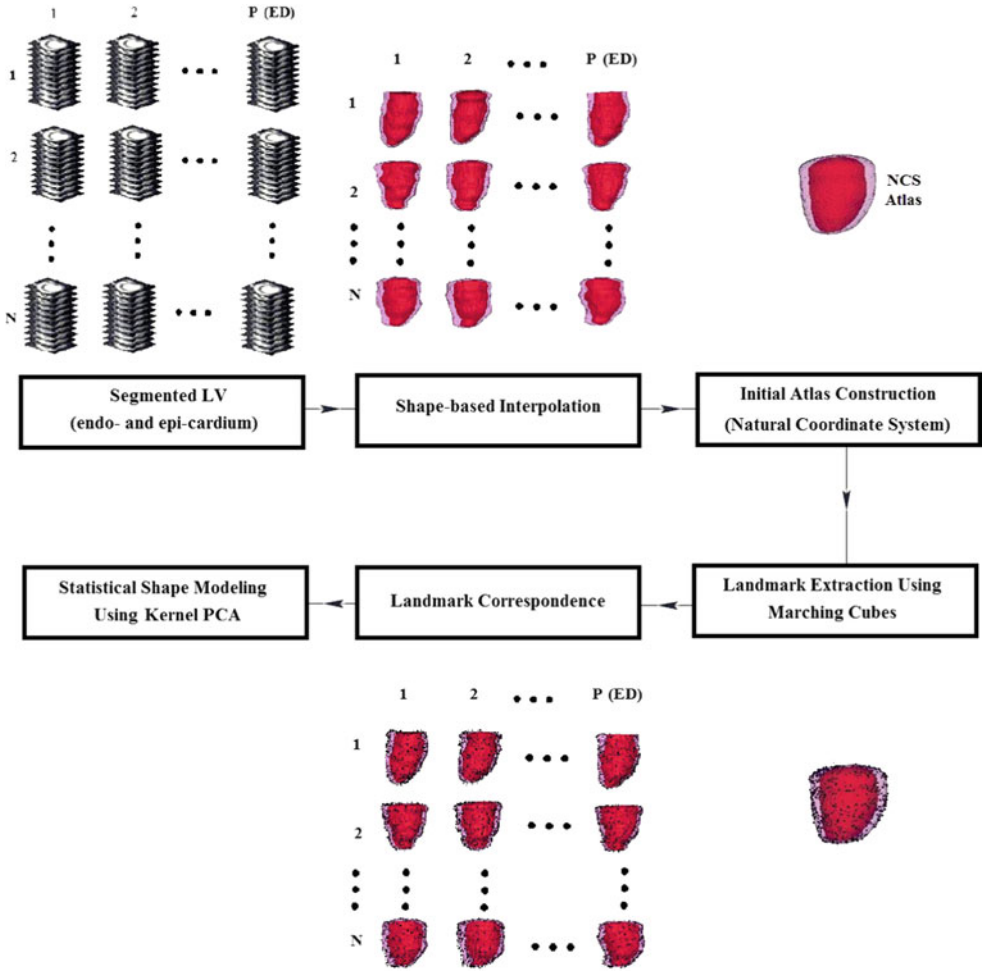

Fig. 1 The block diagram of proposed 4D statistical shape model. It consists of the preprocessing, landmark extraction and statistical shape modeling steps

capacity and generalization ability measures. These customary measures are assessed in statistical shape modeling studies [9]. The LV segmentation result of 4D KPCA-based active shape model is compared with the conventional ASM. In the result and discussion section, we provide results demonstrating the validity of our approach and a critical assessment of the method. In the last section, we conclude the paper.

Methods

This section describes our approach for model construction of the cardiac left ventricle using KPCA. The whole modeling procedure is summarized in Fig. 1. In the following, each step is described in detail.

I. Preprocessing

Due to breathing artifact, the spatial slices should be aligned. We apply the method proposed by Andreopoulos et al. [31] to correct the misalignment of spatial data. They employed a simple registration algorithm to find the necessary translation of short-axis slices. The median slice is chosen as the first reference slice and the rigid registration with 2 degrees of freedom (translation in X and Y direction) is applied for artifact correction. Once all the slices above the median slice are shifted by the rigid transform, the next upper slice is chosen as the reference and the process is repeated for all slices above it. The whole procedure is repeated for the slices below the median slice. Figure 2 shows the short-axis and the simulated long-axis views of a sample cardiac MR data before and after the breath-hold correction.

As it is clear in Fig. 2, a significant staircase artifact in the direction of the long axis of the heart is generated for the manual segmentation. This occurs because of the large voxel anisotropy in MR short-axis acquisitions of functional cardiac data sets. To reduce those artifacts, shape-based interpolation is applied to all frames of a cardiac cycle to obtain labeled images of isotropic voxel size [32]. The method used segmented dataset was as an extension of Raya and Udupa's

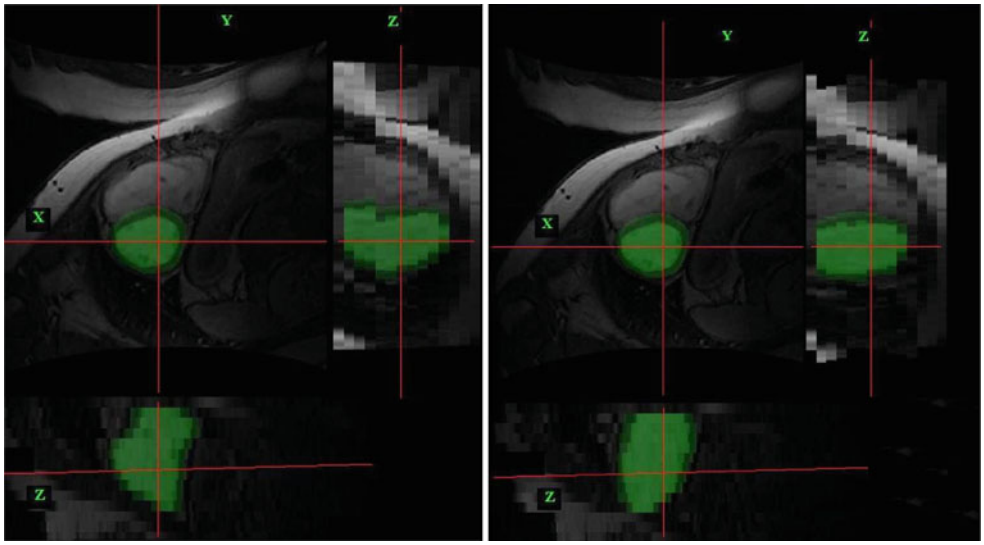

Fig. 2 An example of the short-axis MR image and its simulated long axes views before (*left*) and after (*right*) the breath-hold correction. The manual segmentation result for the blood pool (*light green*) and the myocardium (*dark green*) is superimposed on the original image

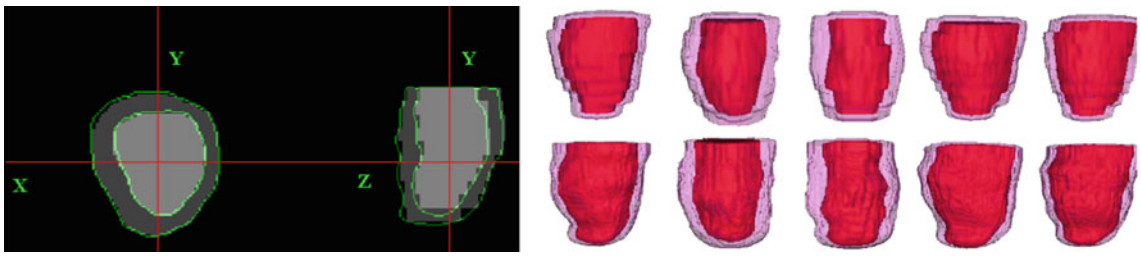

Fig. 3 Superposition of the shape-based interpolated LV walls (*green contours*) on the manually segmented ones (*gray*) (*left*), surface rendering of manually segmented LV walls (*right*, *up*) and interpolated LV walls (*right*, *down*) for some phases of a cardiac cycle

shape-based interpolation [33]. It is applied for each 3D shape in all phases of a cardiac cycle. In each 3D shape, a 2D distance map is constructed for each slice. These maps are interpolated and translated back to the binary image. The superposition of shape-based interpolated data on the manually segmented images can be seen in Fig. 3. The 3D visualization of the segmented and resampled data is also shown in this figure. Several authors utilized this method for isotropic voxel generation of manually segmented data [14,16,17].

II. Landmark generation

To construct the SSM, a set of correspondent landmarks should be found over all frames of all datasets. Two main approaches for landmark extraction in 4D cardiac images are arc-length resampling [18,22] and propagating pseudo-landmarks from an initial atlas [17,19] or an arbitrary frame [20] to all frames.

We adopted the method proposed by Frangi et al. [14] to construct an initial atlas in a natural coordinate system (NCS) for the end-diastolic phase. This makes the final landmarks not be biased toward any training sample. The initial atlas building procedure is composed of the following steps:

1. Choose one segmented training sample to be an initial atlas.
2. Align all samples with the atlas by using an affine transformation.
3. Make the average image by shape-based blending of all aligned images.
4. The average image is the atlas in the reference coordinate system (RCS). To reduce the bias toward the selected initial training sample, the process from step 2 is repeated by altering the atlas with the obtained average image. The process terminate when the difference between two consecutive atlases is small.
5. Transform all aligned samples in step 2 to the RCS atlas using a non-rigid deformation field. The average of all deformations is calculated and applied to the RCS atlas. The new image is the atlas in Natural Coordinate System (NCS).

We modify the proposed method by Zhu et al. [20] by exploiting the initial atlas. Let $\{x_{ij} : i = 1, \ldots, N_p; j = 1, \ldots, N_f\}$ denote $N = N_p \times N_f$ shapes. There are N_f frames for each of N_p subjects. The landmark extraction procedure is shown in Fig. 4. It is composed of the following steps:

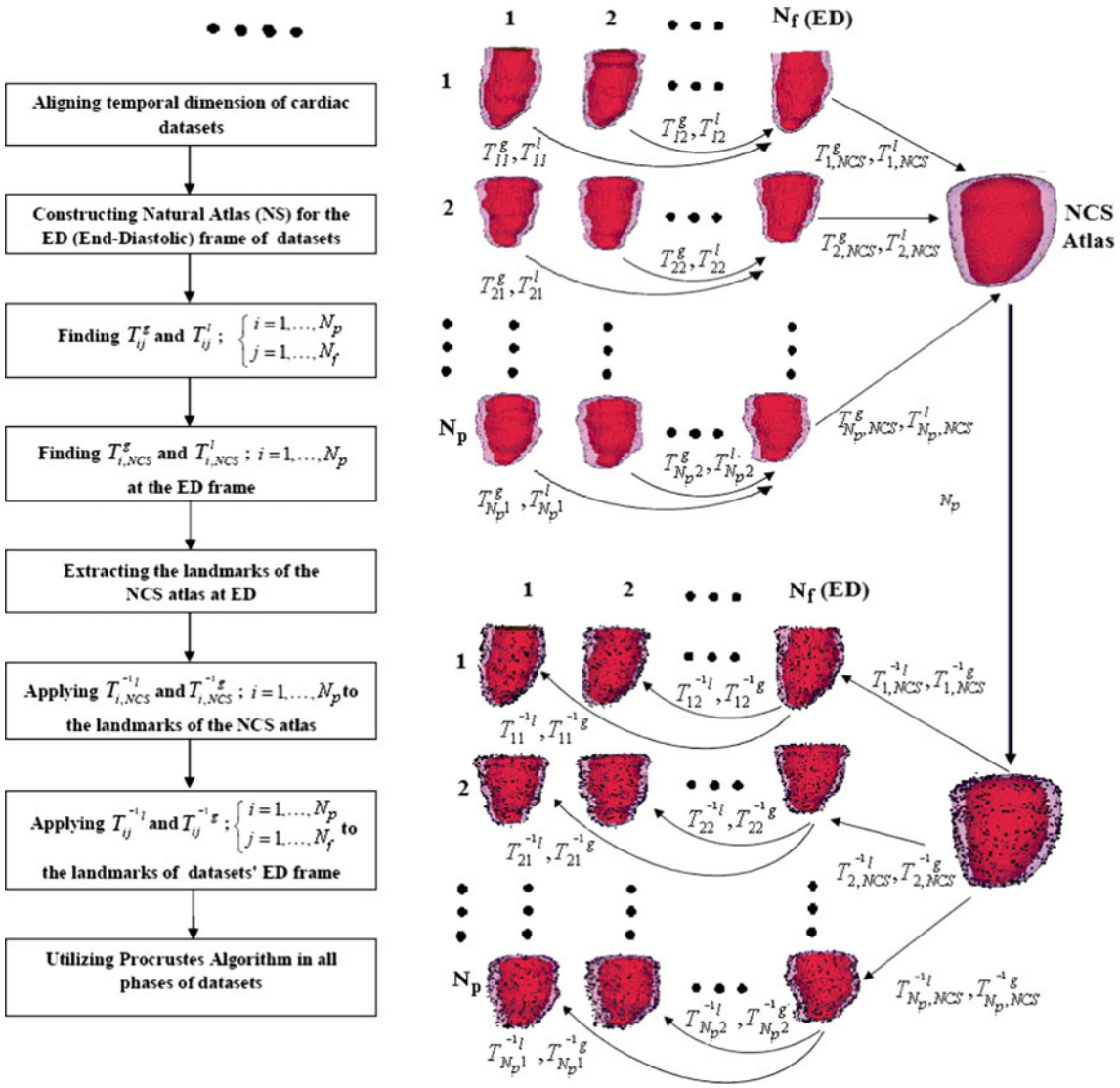

Fig. 4 The block diagram of proposed corresponding landmark extraction method. The initial atlas in natural coordinate system is built for the end-diastolic phase. The landmarks extracted from it are propagated to all frames of all datasets using the local and global transformation from all phases of each dataset to its end-diastolic phase (T_{ij}^{g}, T_{ij}^{l}) and from each end-diastolic phase to the NCS atlas ($T_{i,\mathrm{NCS}}^{\mathrm{g}} T_{i,\mathrm{NCS}}^{\mathrm{l}}$)

1. After aligning the end-diastolic frames of all sequences using electrocardiogram (ECG) signal, shape-based or registration-based interpolation is used to generate same number of frames for all datasets. As all datasets utilized in this paper consist of exactly 20 frames, this step is ignored in our work.
2. The initial atlas in the natural coordinate system is built for the end-diastolic phase.
3. By finding global (T_{ij}^{g}) and local (T_{ij}^{l}) transformations ($i = 1, \ldots, N_{\mathrm{p}}$; $j = 1, \ldots, N_{\mathrm{f}}$), all frames of each dataset are aligned to their correspondent end-diastolic phase. An affine transformation is used for global transformation while the local transformation is presented by a non-rigid free-form deformation [10].
4. The end-diastolic phase of all datasets is aligned to the initial atlas by a global ($T_{i,\mathrm{NCS}}^{\mathrm{g}}$) and a local ($T_{i,\mathrm{NCS}}^{\mathrm{l}}$) transformation ($i = 1, \ldots, N_{\mathrm{p}}$).
5. The marching cubes algorithm is utilized to generate a dense triangulation of the boundary surface of the initial atlas [34]. The number of nodes of mesh is too high after applying marching cubes algorithm to the initial atlas. We utilize VTK's decimation technique to reduce the number of the landmarks [35]. It reduces the number of triangles in a mesh while preserving the shape and topology as good as possible. Besides, to reduce the effect of staircase artifact and avoid producing many narrow and long triangles in the decimated surface, the mesh is smoothed before the decimation.

6. The obtained pseudo-landmarks in stage 5 are propagated to the surface of all end-diastolic samples. This is achieved by exploiting the inverse of local and global transformations in stage 4 ($T_{i,\mathrm{NCS}}^{-1\mathrm{l}}$, $T_{i,\mathrm{NCS}}^{-1\mathrm{g}}$).
7. The landmarks of all frames are obtained by applying the inverse of transformations ($T_{ij}^{-1\mathrm{l}}$, $T_{ij}^{-1\mathrm{g}}$) in stage 3 to the landmarks of the end-diastolic phase. We do this for each dataset.
8. All auto-landmarked shapes are aligned to a reference coordinate system using Procrustes algorithm [36].

III. Statistical shape modeling

In the following, we describe linear PDM for 4D statistical modeling. Then, we introduce the nonlinear SSM algorithm using KPCA. As mentioned earlier, $\{x_{ij} : i = 1, \ldots, N_\mathrm{p}; j = 1, \ldots, N_\mathrm{f}\}$ denote $N = N_\mathrm{p} \times N_\mathrm{f}$ shapes. There are N_f frames for each of N_p subjects. Each shape consists of m $3D$landmarks, $\{\mathbf{P}_k = (P_{1k}, P_{2k}, P_{3k}); k = 1, 2, \ldots, m\}$, represented by the vector $(P_{11}, P_{21}, P_{31}, P_{12}, P_{22}, P_{32}, \ldots, P_{1m}, P_{2m}, P_{3m})$, a point in a $3mD$space.

4D linear point distribution model

PCA-based PDM To construct a linear PCA-based PDM, an $3mD$ ellipsoid is fitted to the landmarks by principal component analysis. The principal axes of the ellipsoid show the modes of variation. To accomplish this, the covariance matrix of the data is computed. Then, the eigenvectors (ϕ_α) and eigenvalues ($\omega_\alpha^{(\mathrm{PCA})}$) of the covariance matrix are extracted. ϕ_α and $\omega_\alpha^{(\mathrm{PCA})}$ show the direction and the variance of the variation in the $3mD$space. By sorting the eigenvalues ($\omega_\alpha^{(\mathrm{PCA})} \geq \omega_{\alpha+1}^{(\mathrm{PCA})}$) and putting their corresponding eigenvectors in the columns of the matrix $\Phi^{(\mathrm{PCA})} = (\phi_1 | \phi_2 | \cdots)$, the linear model is achieved:

$$x = \bar{x} + \Phi^{(\mathrm{PCA})}\mathbf{e}^{(\mathrm{PCA})} \tag{1}$$

where $\bar{x}$ is the average landmark vector, $\mathbf{e}^{(\mathrm{PCA})}$ is the shape parameter vector of the model, which is given by $\mathbf{e}^{(\mathrm{PCA})} = \mathbf{\Phi}^{(\mathrm{PCA})^T}(x - \bar{x})$. Usually, the largest $M^{(\mathrm{PCA})}$ eigenvalues are selected and the shapes are approximated by them. By applying limits of $\pm 3\sqrt{\omega_\alpha^{(\mathrm{PCA})}}$ to the parameter e_α(α^{th} parameter of the vector $\mathbf{e}^{(\mathrm{PCA})}$), we are sure that the shape generated is similar to those in the original training set. The covariance matrix for the total shape distribution is given by:

$$C_{\mathrm{total}}^{(\mathrm{PCA})} = \frac{1}{N_\mathrm{p}N_\mathrm{f}} \sum_{i=1}^{N_\mathrm{p}} \sum_{j=1}^{N_\mathrm{f}} \left(x_{ij} - \bar{x}\right)\left(x_{ij} - \bar{x}\right)^T \tag{2}$$

where $\bar{x} = \frac{1}{N_\mathrm{p}N_\mathrm{f}} \sum_{i=1}^{N_\mathrm{p}} \sum_{j=1}^{N_\mathrm{f}} x_{ij}$ is the total mean. Like in the work of Perperidis et al. [17], we identify what changes in the cardiac anatomy occur due to the cardiac cycle (intra-subject distribution) and what changes occur due to shape variation across the population (inter-subject distribution). They utilized 2 different covariance matrices for the variations due to the cardiac cycle ($C_{\mathrm{within}}^{\mathrm{old(PCA)}}$) and the differences across the population ($C_{\mathrm{between}}^{(\mathrm{PCA})}$) as follows:

$$C_{\mathrm{within}}^{\mathrm{old(PCA)}} = \frac{1}{N_\mathrm{p}N_\mathrm{f}} \sum_{i=1}^{N_\mathrm{p}} \sum_{j=1}^{N_\mathrm{f}} \left(x_{ij} - \bar{x}_i\right)\left(x_{ij} - \bar{x}_i\right)^T \tag{3}$$

$$C_{\mathrm{between}}^{(\mathrm{PCA})} = \frac{1}{N_\mathrm{p}} \sum_{i=1}^{N_\mathrm{p}} \left(\bar{x}_i - \bar{x}\right)\left(\bar{x}_i - \bar{x}\right)^T \tag{4}$$

where $\bar{x}_i$ is the average of the frames for the subject i. We change the equation for the covariance matrix of intra-subject distribution as

$$C_{\mathrm{within}}^{\mathrm{new(PCA)}} = \frac{1}{N_\mathrm{f}} \sum_{j=1}^{N_\mathrm{f}} \left(\bar{x}_j - \bar{x}\right)\left(\bar{x}_j - \bar{x}\right)^T \tag{5}$$

where $\bar{x}_j$ is the average of the subjects for the frame j. The major reason for proposing Eq. (5) instead of Eq. (3) is that its structure is more similar to Eq. (4). As Eq. (4) shows the distribution of the frames' mean across the population, it is obvious that Eq. (5) implies the variation of subjects' mean due to the cardiac cycle. Besides, the calculation of eigenvalues and eigenvectors is quicker using Eq. (5). The covariance matrix $C_{\mathrm{within}}^{\mathrm{new(PCA)}}$ is $3m \times 3m$, which is very large. However, we can compute them from a smaller $N_\mathrm{f} \times N_\mathrm{f}$ matrix using the method explained by Cootes et al. in the appendix A of [37].

ICA-based PDM The goal of ICA is to find the independent non-Gaussian components from the mixed signals [24]. ICA does not assume a Gaussian distribution of the input data. The linear ICA-based PDM can be expressed as follows:

$$x = \bar{x} + \Phi^{(\mathrm{ICA})}\mathbf{e}^{(\mathrm{ICA})} \tag{6}$$

where $\Phi^{(\mathrm{ICA})}$ is the mixing matrix with $M^{(\mathrm{ICA})}$ number of components and $\mathbf{e}^{(\mathrm{ICA})}$ is the source signal. ICA is applied to estimate the mixing matrix and statistically independent source signals. Different methods exist to calculate them such as FastICA, InfoMax, and JADE. To sort the independent components, several methods proposed by Uzumcu et al. [24]. We calculate the alignment of shapes with independent components. To accomplish this, they are considered as vectors in shape space. The mean angle between each component and the shape set is calculated, and the components are sorted with increasing mean angle. The limits of $\pm 3\sigma^{(\mathrm{ICA})}$ ($\sigma^{(\mathrm{ICA})}$ is the standard deviation of the independent components) is applied to the parameter e_α(αth parameter of the

vector $\mathbf{e}^{(\mathrm{ICA})}$) to generate similar shapes to the training samples. The inter-subject and intra-subject distribution of the 4D datasets is modeled as follows:

$$\begin{aligned} x_{\text{between}} &= \bar{x} + \Phi^{(\mathrm{ICA})}_{\text{between}} \mathbf{e}^{(\mathrm{ICA})}_{\text{between}} \\ x_{\text{within}} &= \bar{x} + \Phi^{(\mathrm{ICA})}_{\text{within}} \mathbf{e}^{(\mathrm{ICA})}_{\text{within}} \end{aligned} \tag{7}$$

where $\Phi^{(\mathrm{ICA})}_{\text{between}}$ and $\mathbf{e}^{(\mathrm{ICA})}_{\text{between}}$ are the mixing matrix and the source signal for the average of the frames in each subject ($\bar{x}_i$). $\Phi^{(\mathrm{ICA})}_{\text{within}}$ and $\mathbf{e}^{(\mathrm{ICA})}_{\text{within}}$ are the mixing matrix and the source signal for the average of the subjects in each frame.

4D Nonlinear Point Distribution Model KPCA is utilized to model the variation of population for two reasons:

1. It does not need to assume a multidimensional Gaussian distribution for the cloud of landmark vectors.
2. KPCA is a powerful technique for extracting the nonlinear variation of the training samples.

This is achieved by nonlinear mapping of shapes to a new feature space that is supposed linear. We will describe this space H, which is related to the input space by a nonlinear map:

$$\begin{aligned} &\Psi : R^{3m} \rightarrow H \\ &x_{ij} \rightarrow \Psi\left(x_{ij}\right) \end{aligned} \tag{8}$$

Now, the covariance matrices for the inter-subject ($C^{(\mathrm{KPCA})}_{\text{between}}$) and intra-subject ($C^{(\mathrm{KPCA})}_{\text{within}}$) distributions can be calculated in space H as follows:

$$\begin{aligned} C^{(\mathrm{KPCA})}_{\text{between}} &= \frac{1}{N_\mathrm{p}} \sum_{i=1}^{N_\mathrm{p}} \left(\tilde{\Psi}\left(\bar{x}_i\right)\right)\left(\tilde{\Psi}\left(\bar{x}_i\right)\right)^T \\ C^{(\mathrm{KPCA})}_{\text{within}} &= \frac{1}{N_\mathrm{f}} \sum_{j=1}^{N_\mathrm{f}} \left(\tilde{\Psi}\left(\bar{x}_j\right)\right)\left(\tilde{\Psi}\left(\bar{x}_j\right)\right)^T \end{aligned} \tag{9}$$

where $\tilde{\Psi}(\bar{x}_i) = \Psi(\bar{x}_i) - \frac{1}{N_\mathrm{p}} \sum_{r=1}^{N_\mathrm{p}} (\Psi(\bar{x}_r))$ and $\tilde{\Psi}(\bar{x}_j) = \Psi(\bar{x}_j) - \frac{1}{N_\mathrm{f}} \sum_{s=1}^{N_\mathrm{f}} (\Psi(\bar{x}_s))$. The major drawback is the high-dimensionality of the feature space H that makes the calculation of principal axes very complicated and time-consuming. It is important to note that applying PCA in H only needs the dot products of the $\Psi(\bar{x}_i)$ or $\Psi(\bar{x}_j)$. To solve the problem, kernel functions for intra-subject and inter-subject distribution are defined as:

$$\begin{aligned} K_{\text{between}}(\bar{x}_{i_1}, \bar{x}_{i_2}) &= \left\langle \Psi\left(\bar{x}_{i_1}\right), \Psi\left(\bar{x}_{i_2}\right)\right\rangle = \Psi\left(\bar{x}_{i_1}\right)^T \Psi\left(\bar{x}_{i_2}\right); \\ &\quad (i_1, i_2 = 1, \ldots, N_\mathrm{p}) \\ K_{\text{within}}(\bar{x}_{j_1}, \bar{x}_{j_2}) &= \left\langle \Psi\left(\bar{x}_{j_1}\right), \Psi\left(\bar{x}_{j_2}\right)\right\rangle = \Psi\left(\bar{x}_{j_1}\right)^T \Psi\left(\bar{x}_{j_2}\right); \\ &\quad (j_1, j_2 = 1, \ldots, N_\mathrm{f}) \end{aligned} \tag{10}$$

This allows us to compute the value of dot product in H without performing the mapping to the feature space. In summary, the following steps are necessary to compute principal components using KPCA:

1. Calculating the un-normalized kernel matrices that consist of kernel functions as their elements

$$\begin{aligned} \mathbf{K}^{\text{between}}_{i_1 i_2} &= K_{\text{between}}\left(\bar{x}_{i_1}, \bar{x}_{i_2}\right) \quad \left(i_1, i_2 = 1, \ldots, N_\mathrm{p}\right) \\ \mathbf{K}^{\text{within}}_{j_1 j_2} &= K_{\text{within}}\left(\bar{x}_{j_1}, \bar{x}_{j_2}\right) \quad (j_1, j_2 = 1, \ldots, N_\mathrm{f}) \end{aligned} \tag{11}$$

2. Computing the normalized kernel matrices from the un-normalized ones:

$$\begin{aligned} \tilde{\mathbf{K}}^{\text{between}} &= \mathbf{H}^{\text{between}} \mathbf{K}^{\text{between}} \mathbf{H}^{\text{between}}, \\ &\quad \mathbf{H}^{\text{between}} = \mathbf{I}_{N_\mathrm{p}} - \frac{1}{N_\mathrm{p}} \mathbf{1}_{N_\mathrm{p}} \mathbf{1}^t_{N_\mathrm{p}}, \\ &\quad \mathbf{1}_{N_\mathrm{p}} = [1, \ldots, 1]^t_{N_\mathrm{p} \times 1} \\ \tilde{\mathbf{K}}^{\text{within}} &= \mathbf{H}^{\text{within}} \mathbf{K}^{\text{within}} \mathbf{H}^{\text{within}}, \\ &\quad \mathbf{H}^{\text{within}} = \mathbf{I}_{N_\mathrm{f}} - \frac{1}{N_\mathrm{f}} \mathbf{1}_{N_\mathrm{f}} \mathbf{1}^t_{N_\mathrm{f}}, \\ &\quad \mathbf{1}_{N_\mathrm{f}} = [1, \ldots, 1]^t_{N_\mathrm{f} \times 1} \end{aligned} \tag{12}$$

3. Finding the eigenvalues (λ^{between} and λ^{within}) and eigenvectors ($\mathbf{b}^{\text{between}}$ and $\mathbf{b}^{\text{within}}$) of Kernel matrices and normalizing the eigenvectors:

$$\begin{aligned} \lambda^{\text{between}}_\alpha b(i)^{\text{between}}_\alpha &= \frac{1}{N_\mathrm{p}} \sum_{r=1}^{N_\mathrm{p}} \tilde{\mathbf{K}}^{\text{between}}_{ri} b(r)^{\text{between}}_\alpha \\ &\quad \times \alpha = 1, \ldots, M^{(\mathrm{KPCA})}_{\text{between}} \\ \lambda^{\text{within}}_\beta b(j)^{\text{within}}_\beta &= \frac{1}{N_\mathrm{f}} \sum_{s=1}^{N_\mathrm{f}} \tilde{\mathbf{K}}^{\text{within}}_{sj} b(s)^{\text{within}}_\beta \\ &\quad \times \beta = 1, \ldots, M^{(\mathrm{KPCA})}_{\text{within}} \end{aligned} \tag{13}$$

where $b(i)^{\text{between}}_\alpha = \mathbf{b}^{\text{between}}_\alpha \bullet \tilde{\Psi}(\bar{x}_i)$ and $b(j)^{\text{within}}_\beta = \mathbf{b}^{\text{within}}_\beta \bullet \tilde{\Psi}(\bar{x}_j)$. The most $M^{(\mathrm{KPCA})}_{\text{between}}$ and $M^{(\mathrm{KPCA})}_{\text{within}}$ eigenvalues are selected so that the model denotes some proportion of the total variance.

4. Extracting the principal components of sample y by computing projections onto the eigenvectors:

$$\begin{aligned} \mathrm{KPCA}^{\text{between}}_\alpha(y) &= \sum_{i=1}^{N_\mathrm{p}} b(i)^{\text{between}}_\alpha K_{\text{between}}(\bar{x}_i, y), \\ &\quad \alpha = 1, \ldots, M^{(\mathrm{KPCA})}_{\text{between}} \end{aligned}$$

$$\mathrm{KPCA}_{\beta}^{\mathrm{within}}(y)=\sum_{j=1}^{N_{\mathrm{f}}} b(j)_{\beta}^{\mathrm{within}} K_{\mathrm{within}}\left(\bar{x}_j, y\right),$$
$$\beta = 1, \ldots, M_{\mathrm{within}}^{(\mathrm{KPCA})} \tag{14}$$

Some commonly used kernel functions are as follows: polynomial, radial basis function (RBF) or Gaussian, sigmoid. For more details, see [38]. The important thing in applying KPCA for statistical modeling is how to constrain the model parameters and define the proximity to data according to the utilized kernel function [39]. Although the parameter constraints for polynomial kernel are similar to linear PCA, but this is not valid or RBF and sigmoid kernels. For instance, consider the RBF kernel as follows:

$$K_{\mathrm{between}}(y,\bar{x}_i)=\exp\left(-\frac{\|y-\bar{x}_i\|^2}{2\sigma_{\mathrm{between}}^2}\right)\quad (i=1,\ldots,N_{\mathrm{p}})$$
$$K_{\mathrm{within}}(y,\bar{x}_j)=\exp\left(-\frac{\|y-\bar{x}_j\|^2}{2\sigma_{\mathrm{within}}^2}\right)\quad (j=1,\ldots,N_{\mathrm{f}}) \tag{15}$$

where $\sigma_{\mathrm{between}}$ and σ_{within} are the width of the Gaussian kernels. Following from (13), it can be seen that the principal components for the sample (y) far from all training data ($\bar{x}_i$ or $\bar{x}_j$) are almost zero (this occurs for the average data in linear PCA).

We exploit the pseudo-density function ($\hat{\rho}_{\mathrm{between}}(x)$ and $\hat{\rho}_{\mathrm{within}}(x)$), which was defined by Davies et al. [38] to attain the acceptable shape for statistical modeling as follows:

$$\begin{aligned}
\hat{\rho}_{\mathrm{between}}(x) &= \frac{1}{A_{\mathrm{between}}}\sum_{r_1,r_2=1}^{N_{\mathrm{p}}}\sum_{\alpha=1}^{M_{\mathrm{between}}^{(\mathrm{KPCA})}} b(r_1)_{\alpha}^{\mathrm{between}} b(r_2)_{\alpha}^{\mathrm{between}} \\
&\quad \times K_{\mathrm{between}}\left(x,x_{r_1}\right) K_{\mathrm{between}}\left(x,x_{r_2}\right) \\
A_{\mathrm{between}} &= \sigma_{\mathrm{between}}^{M_{\mathrm{between}}^{(\mathrm{KPCA})}} \pi^{M_{\mathrm{between}}^{(\mathrm{KPCA})}/2} \mathrm{trace}\left(\sqrt{\mathbf{K}^{\mathrm{between}}}\mathbf{B}^{\mathrm{between}}\right), \\
\mathbf{B}_{r_1r_2}^{\mathrm{between}} &= \sum_{\alpha=1}^{M_{\mathrm{between}}^{(\mathrm{KPCA})}} b(r_1)_{\alpha}^{\mathrm{between}} b(r_2)_{\alpha}^{\mathrm{between}}
\end{aligned} \tag{16}$$

$$\begin{aligned}
\hat{\rho}_{\mathrm{within}}(x) &= \frac{1}{A_{\mathrm{within}}}\sum_{s_1,s_2=1}^{N_{\mathrm{f}}}\sum_{\beta=1}^{M_{\mathrm{within}}^{(\mathrm{KPCA})}} b(s_1)_{\beta}^{\mathrm{within}} b(s_2)_{\beta}^{\mathrm{within}} \\
&\quad \times K_{\mathrm{within}}\left(x,x_{s_1}\right) K_{\mathrm{within}}\left(x,x_{s_2}\right) \\
A_{\mathrm{within}} &= \sigma_{\mathrm{within}}^{M_{\mathrm{within}}^{(\mathrm{KPCA})}} \pi^{M_{\mathrm{within}}^{(\mathrm{KPCA})}/2} \mathrm{trace}\left(\sqrt{\mathbf{K}^{\mathrm{within}}}\mathbf{B}^{\mathrm{within}}\right), \\
\mathbf{B}_{s_1s_2}^{\mathrm{within}} &= \sum_{\beta=1}^{M_{\mathrm{within}}^{(\mathrm{KPCA})}} b(s_1)_{\beta}^{\mathrm{within}} b(s_2)_{\beta}^{\mathrm{within}}
\end{aligned} \tag{17}$$

They show the distance from the origin in KPCA space and have a strict upper bound. To generate shapes similar to those in the original training set, the lower bound should be located on it.

To evaluate the nonlinear statistical model and use it in image segmentation, the pre-image should be reconstructed by the reverse mapping from the feature space H back to the input space. Mika et al. [40] proposed a fixed-point iterative method that was dependent to the initial guess and was numerically unstable. To solve these problems, a different approach was presented by Kwok et al. [41] based on distance constraints in the space H. Rathi et al. [42] adopted the latter method and modified it by suggesting a simple algebraic formulation. We utilize their method for calculation of generalization ability and specificity measures. The pre-image for inter-subject ($\hat{x}_{\mathrm{between}}$) and intra-subject distribution ($\hat{x}_{\mathrm{within}}$) is obtained for the RBF kernel as follows:

$$\begin{cases}
\hat{x}_{\mathrm{between}} \approx \dfrac{\sum_{i=1}^{N_{\mathrm{p}}} \tilde{\gamma}_i^{\mathrm{between}}\left(\frac{1}{2}\left(2-\tilde{d}^2(P_{\Psi}(x_{\mathrm{between}}),\Psi(\bar{x}_i))\right)\right)\bar{x}_i}{\sum_{i=1}^{N_{\mathrm{p}}} \tilde{\gamma}_i^{\mathrm{between}}\left(\frac{1}{2}\left(2-\tilde{d}^2(P_{\Psi}(x_{\mathrm{between}}),\Psi(\bar{x}_i))\right)\right)} \\
\hat{x}_{\mathrm{within}} \approx \dfrac{\sum_{j=1}^{N_{\mathrm{f}}} \tilde{\gamma}_j^{\mathrm{within}}\left(\frac{1}{2}\left(2-\tilde{d}^2(P_{\Psi}(x_{\mathrm{within}}),\Psi(\bar{x}_j))\right)\right)\bar{x}_j}{\sum_{j=1}^{N_{\mathrm{f}}} \tilde{\gamma}_j^{\mathrm{within}}\left(\frac{1}{2}\left(2-\tilde{d}^2(P_{\Psi}(x_{\mathrm{within}}),\Psi(\bar{x}_j))\right)\right)}
\end{cases} \tag{18}$$

where the values of $\tilde{\gamma}_i^{\mathrm{between}}$ and $\tilde{\gamma}_j^{\mathrm{within}}$ are given by:

$$\begin{cases}
\tilde{\gamma}_i^{\mathrm{between}} = \gamma_i^{\mathrm{between}} + \frac{1}{N_{\mathrm{p}}}\left(\mathbf{1}_{N_{\mathrm{p}}} - \sum_{r=1}^{N_{\mathrm{p}}} \gamma_r^{\mathrm{between}}\right), \\
\gamma_i^{\mathrm{between}} = \sum_{\alpha=1}^{M_{\mathrm{between}}^{(\mathrm{KPCA})}} \mathrm{KPCA}_{\alpha}^{\mathrm{between}} b(i)_{\alpha}^{\mathrm{between}} \\
\tilde{\gamma}_j^{\mathrm{within}} = \gamma_j^{\mathrm{within}} + \frac{1}{N_{\mathrm{f}}}\left(\mathbf{1}_{N_{\mathrm{f}}} - \sum_{s=1}^{N_{\mathrm{f}}} \gamma_s^{\mathrm{within}}\right), \\
\gamma_j^{\mathrm{within}} = \sum_{\beta=1}^{M_{\mathrm{within}}^{(\mathrm{KPCA})}} \mathrm{KPCA}_{\beta}^{\mathrm{within}} b(j)_{\beta}^{\mathrm{within}}
\end{cases} \tag{19}$$

$P_{\Psi}(x_{\mathrm{between}})$ and $P_{\Psi}(x_{\mathrm{within}})$ are the projection of $\Psi(\cdot)$ onto the subspace of the eigenvectors. Their squared distance from the training set ($\tilde{d}^2(P_{\Psi}(x_{\mathrm{between}}), \Psi(\bar{x}_i))$ and $\tilde{d}^2(P_{\Psi}(x_{\mathrm{within}}), \Psi(\bar{x}_j))$) can be written only in terms of the kernel function [42].

Model evaluation We compare the result of KPCA with linear PCA for evaluation of the nonlinear statistical model. To investigate the statistical behavior of the model, we evaluate its compactness capacity, specificity and generalization ability. "A compact model is one that requires as few parameters as possible for the generation of a valid instance of the modeled object" [16]. The compactness capacity of the shape model, denoted $C(\tau)$, is measured as the cumulated variance (absolute or percentile with respect to the total shape variance) for the first $\tau = 1, \ldots, M$ modes.

$$C(\tau)=\frac{\sum_{t=1}^{\tau}\lambda_t}{\sum_{t=1}^{M}\lambda_t}\times 100;\quad (\tau=1,\ldots,M) \tag{20}$$

"The property of generalization of a shape model measures its ability to represent unseen instances of the object class modeled" [16]. To measure the generalization ability of the model, we build a model from all but one samples of the training dataset and calculate the error of fitting the excluded sample to the constructed model. This process is repeated

Table 1 The details of dataset used in the paper [41]

Number	Pixel spacing (mm per pixel)	Spacing between slices (mm per slice)	Age	Temporal resolution	Short-axis resolution (pixel)
33	0.93–1.64	8–15	2–17	20	256×256

It gives some information about the spacing, age and disease of the subjects. Only 2 datasets have the left ventricular related disease (subjects 22, 27)

for all training samples (leave-one-out test). The algorithm to compute this measure is shown in [38]. It can be defined as a function of the number of parameters $(\tau = 1, \ldots, M)$ as follows:

$$G(\tau) = \frac{1}{N_s} \sum_{u=1}^{N_s} \| w_u(\tau) - z_u \|; \quad (\tau = 1, \ldots, M) \tag{21}$$

where z_u is the training sample that is removed in each iteration of the leave-one-out test and N_s is the number of training dataset. $w_u(\tau)$ is the reconstructed shape using first τ parameters of the constructed model from the training samples with z_u removed. The specificity of a model is defined as how much "it can *only* represent valid instances of the modeled class of object" [38]. This important measure represents the ability of model for image segmentation [38]. It can be defined as a function of the number of parameters $(\tau = 1, \ldots, M)$ as follows:

$$S(\tau) = \frac{1}{N_r} \sum_{u=1}^{N_r} \min_u \left\| v_u(\tau) - z'_u \right\|; \quad (\tau = 1, \ldots, M) \tag{22}$$

where $v_u(\tau)$ is an arbitrary sample generated by the first τ parameters of the model, z'_u is the closest member of training datasets to $v_u(\tau)$ and N_r is the number of samples.

To measure the accuracy of our approach, we used a distance error metric, namely mean absolute distance (MAD) [20]. Let A and Bbe two surfaces to be compared, and supposing they are represented as point sets, that is, $A = \{a_1, a_2, \ldots, a_n\}$ and $B = \{b_1, b_2, \ldots, b_m\}$, we can define MAD as follows:

$$\mathrm{MAD}(A, B) = \frac{1}{2} \left\{ \frac{1}{n} \sum_{i=1}^{n} d(a_i, B) + \frac{1}{m} \sum_{j=1}^{m} d(A, b_j) \right\} \tag{23}$$

where $d(a_i, B) = \min_j \left| b_j - a_i \right|$.

Materials

To evaluate the approach, we utilized the cardiac MR database of a previous work on statistical modeling [31], which was available online with its manual segmentation [43]. It consisted of short-axis cardiac MR image sequences obtained from 33 subjects, all of whom were under the age of 18. The images were scanned with a GE Genesis Signa MR scanner using the FIESTA scan protocol. The detail of the data was shown in the Table 1.

Each patient's image sequence consisted of exactly 20 frames. The number of collected short-axis slices ranged between 8 and 15 per frame. The database consisted of 256×256 pixels with a pixel spacing of 0.93–1.64 mm and a slice distance of 6–13 mm. The epicardial and endocardial contours in each dataset were manually segmented. The basal end of each dataset was indicated by the last slice that showed a complete peripheral endocardial contour. Thus, the mitral valve plane was excluded. We interpolated all manually segmented datasets to an isotropic voxel size with size equal to $1 \times 1 \times 1$ mm^3 per frame. In all 4D images, the LV endocardium and epicardium were manually traced, to provide the ground truth [42]. The papillary muscles were included in the LV blood pool enclosed by the LV endocardial border.

Results

The rigid and non-rigid registrations for building the initial atlas were obtained with the image registration toolkit (IRTK) software [44]. The non-rigid deformation field was represented by a free-form deformation (FFD) based on B-splines [10]. The Kappa statistics was used as a similarity measure for labeled image registrations. This measure varies between zero and one, and values above 0.9 are usually regarded as very good agreements [14]. The standard deviation and mean of the similarity measure for T_{ij}^{g} and T_{ij}^{l} is shown in Fig. 5 over a cardiac cycle. Figure 6 shows the high quality of non-rigid registration for 3 different phases of a cardiac cycle. The final transformed image for the endocardium and epicardium is superimposed on the original image.

To extract the landmarks of the initial atlas, the marching cubes algorithm was applied using VTK software [45]. Then, the nodes of the generated mesh were decimated with the rate equal to 0.98. The number of landmarks before and after decimation is 21,662 and 2408 for epicardium and 14,194 for 1,504 endocardium. Figure 7 shows the shape of the initial atlas before and after decimation.

Before applying KPCA, we calculated the statistical model using PCA. The distribution of 2nd principal component versus 1st principal component for inter-subject

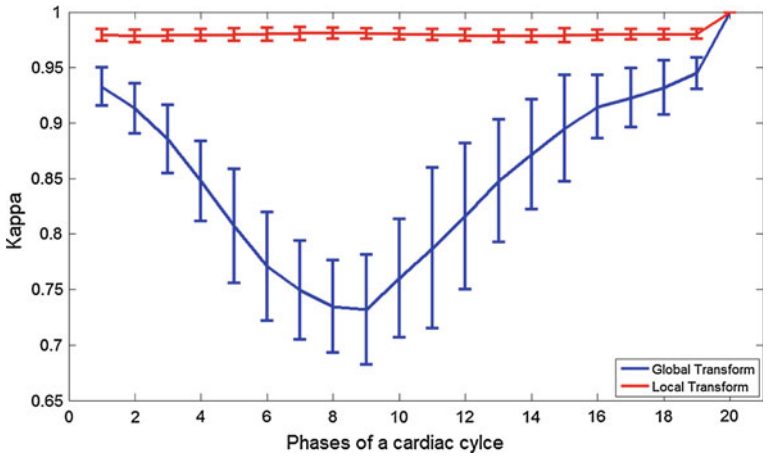

Fig. 5 The standard deviation and mean of the global and local transformations similarity measure ($T_{ij}^{\mathrm{g}}, T_{ij}^{\mathrm{l}}$ $i = 1, \ldots, N_{\mathrm{p}}$; $j = 1, \ldots, N_{\mathrm{f}}$) over a cardiac cycle in the initial atlas construction step. The kappa statistics was used as the registration measure. The high values of Kappa measure for the local transformations shows the high quality of registration. As all phases of each dataset were registered to its end-diastolic phase, the lowest value of Kappa measure for global transformation is for the end-systolic phase (phase 9)

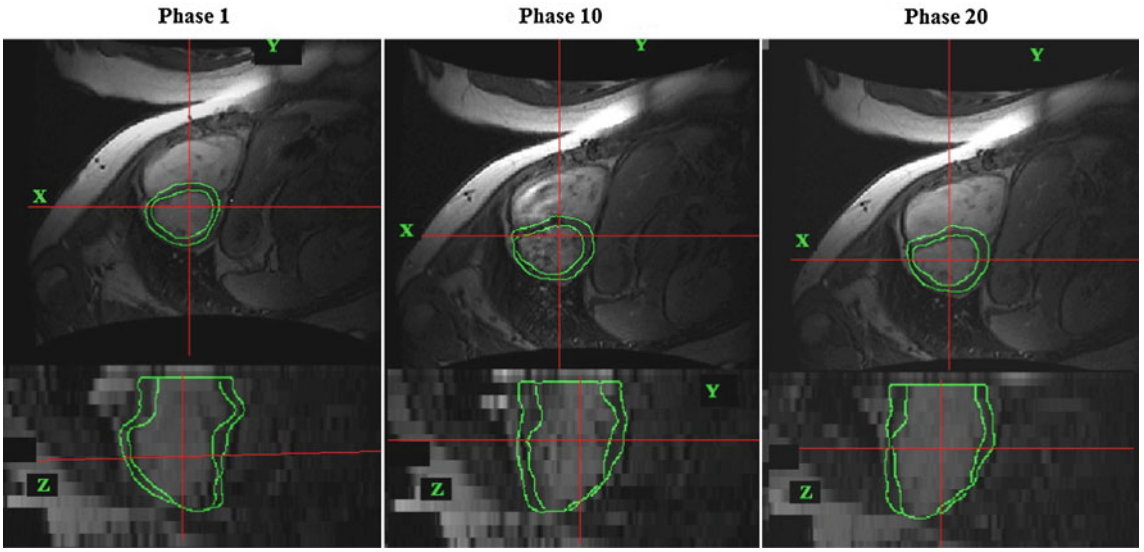

Fig. 6 The result of non-rigid registration for an arbitrary training data over three different phases of a cardiac cycle. The final transformed image for the endocardium and epicardium (*Green edges*) is superimposed on the original image. The results is shown in short-axis (*top row*) and long-axis (*bottom row*) views

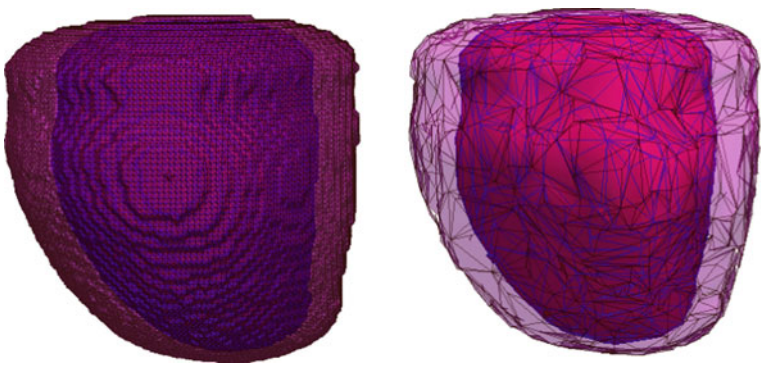

Fig. 7 The triangulation of the initial atlas using marching cubes algorithm (*left*) and the extraction of landmarks after decimating the nodes of the mesh (*right*). the nodes of the generated mesh were decimated with the rate equal to 0.98. The shape of the atlas was preserved after the decimation

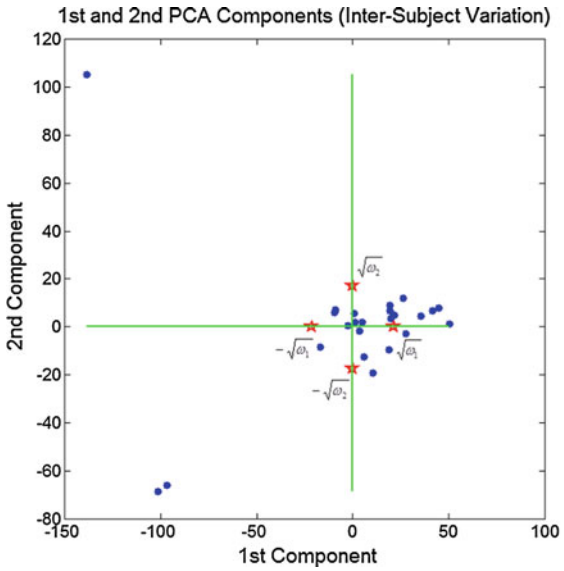

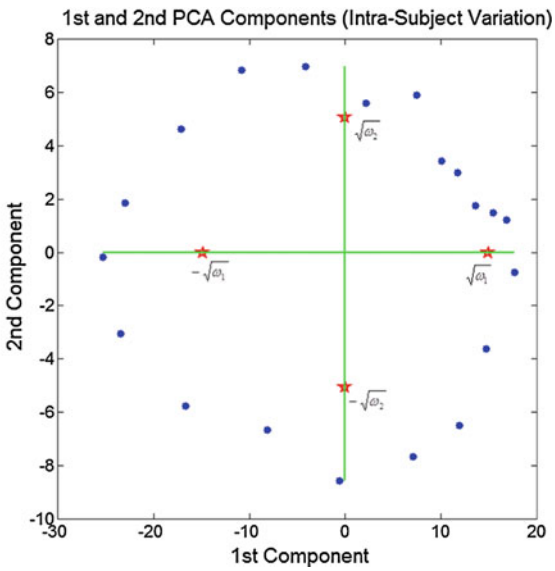

Fig. 8 First and second principal components in the shape C_{between} (*left*) and $C^{\text{new}}_{\text{within}}$ (*right*). Each point represents the value of first and second principal component of a training dataset for PCA-based model. The one standard deviation of the 1st and 2nd component is shown in each figure

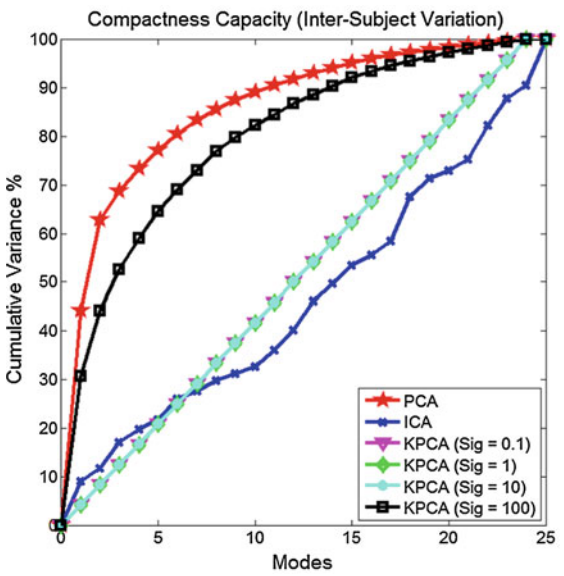

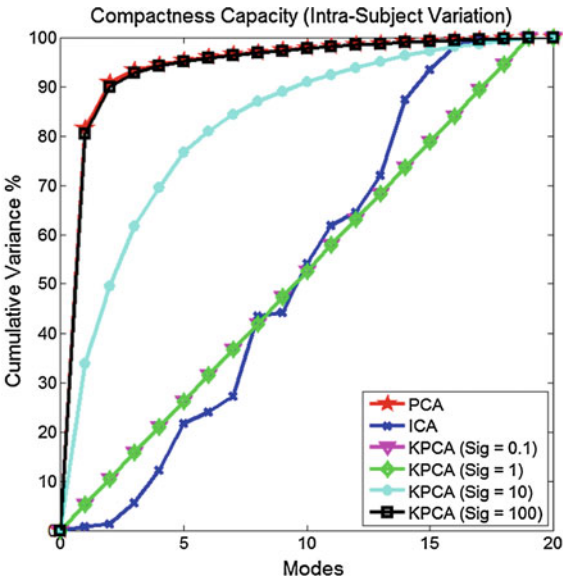

Fig. 9 Percentage of total shape variance versus the number of modes for inter-subject (*left*) and intra-subject (*right*) statistical shape modeling using PCA, ICA and Kernel PCA. The KPCA curve is shown for 4 different value of kernel parameter σ. By the increase of the KPCA curve approaches the PCA curve and by the decrease of it is more similar to the straight line. Generally the KPCA-based model is more compact than ICA-based model

(left) and intra-subject (right) variations is shown in Fig. 8. The probability associated with interval one standard deviation from the origin is equal to 0.68. The one standard deviation of the 1st and 2nd component is shown in the Fig. 7, too. As it is clear in the figure, none of the landmarks is in this interval for intra-subject distribution. The figure shows that the assumption of Gaussian distribution has some limitation for inter-subject and intra-subject distribution.

The "stprtool" toolbox was utilized to compute the KPCA components [46]. The RBF kernel is used in the KPCA framework. "This kernel has been a popular choice in the machine learning community and has proven to nicely extract nonlinear structures from data sets" [28]. We investigate the behavior of the nonlinear model for 4 different values of the kernel parameter ($\sigma = 0.1, 1, 10, 100$). The percentage of total inter-subject and intra-subject shape variance versus the

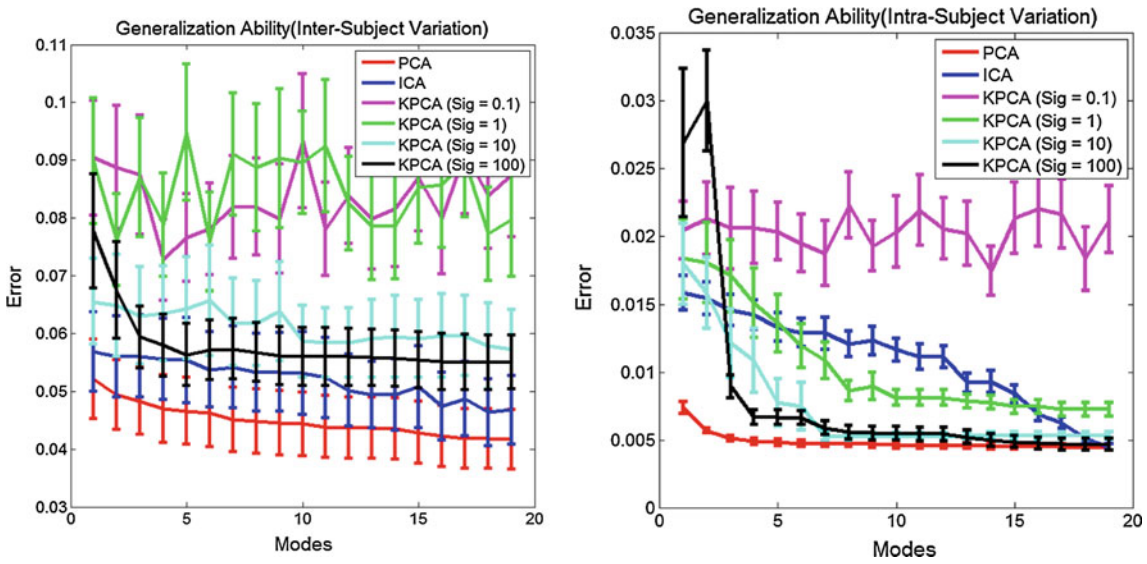

Fig. 10 Reconstruction error versus number of modes in the leave-one-out experiments for inter-subject (*left*) and intra-subject (*right*) statistical shape modeling using PCA, ICA and Kernel PCA. The KPCA curve is shown for 4 different value of the kernel parameter σ. Higher value of the kernel parameter σ decreases the reconstruction error made by KPCA

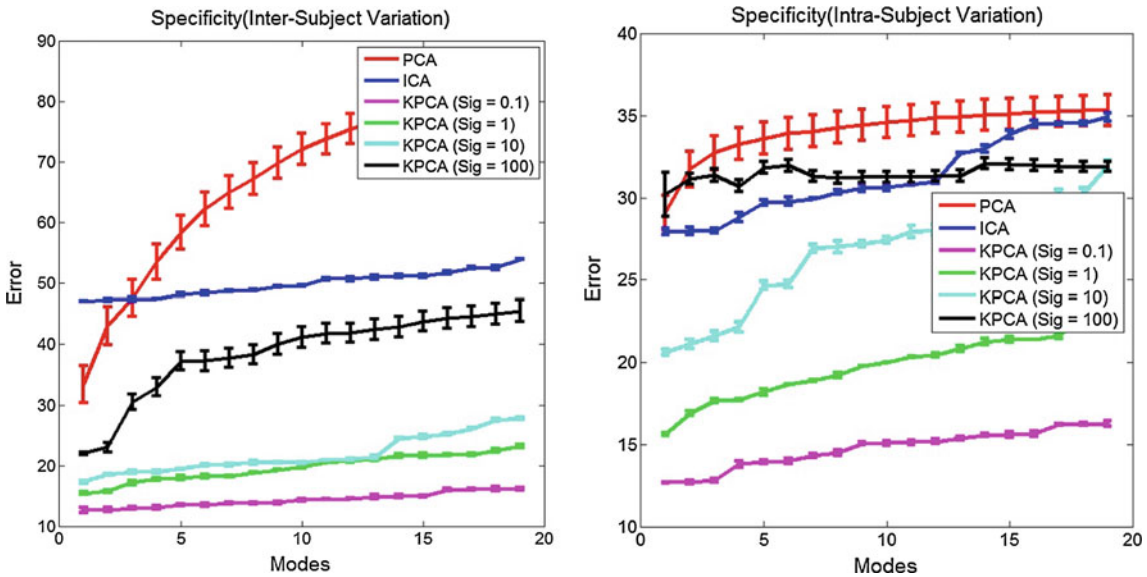

Fig. 11 Specificity for inter-subject (*left*) and intra-subject (*right*) statistical shape modeling using PCA, ICA and Kernel PCA. The KPCA curve is shown for 4 different value of kernel parameter σ. The specificity error of KPCA-based model is lower than ICA-based and PCA-based models for almost all values of parameter σ

number of modes used in statistical shape modeling for PCA, ICA and KPCA is shown in Fig. 9. As we expected, by the increase of σ, the KPCA curve approaches the PCA curve and by the decrease of σ it is more similar to the straight line.

For the leave-one-out experiment, the landmarks of all but one sample were utilized to build the statistical model. This model was subsequently used to reconstruct the excluded sample. This is repeated for all training samples. Finally, the average reconstruction error over the leave-one-out experiments was computed. Figure 10 shows the mean square reconstruction error for KPCA, PCA and ICA as a function of the number of variation modes. For a constant number of modes, the reconstruction error is a little higher for the KPCA-based statistical model. Higher value for kernel parameter decreases the reconstruction error made by KPCA for inter-subject and intra-subject distributions. The generalization ability of the models is nearly the same for the inter-subject distribution.

The specificity for intra-subject and inter-subject distributions is shown in Fig. 11. As it is evident from these figures, the error made by specificity measure is lower for KPCA than PCA and ICA for most values of σ.

To demonstrate the ability of the proposed nonlinear model for cardiac image segmentation, the 4D KPCA-based active shape model was constructed and applied for the LV segmentation of all phases of a cardiac cycle. We utilized the method proposed by Leiner et al. [47] to construct the 4D ASM Model. To build the nonlinear model, KPCA was used instead of PCA. To investigate the effect of σ, segmentation was done for 4 different values of the kernel parameter ($\sigma = 0.1, 1, 10, 100$). The KPCA-based model was built for 20 datasets, and the KPCA-based ASM was applied to the remaining 13 datasets. We used the ASM Toolbox written by Kroon et al. [48] and utilized KPCA instead of PCA for nonlinear model-based segmentation.

Figure 12 shows the regression graph of the proposed method versus manual segmentation. The volume error is measured in cm^3 and shows the absolute difference error of the volume of segmented epicardium and endocardium. The figure shows the result of segmentation for different values of $\sigma(\sigma = 0.1, 1, 10, 100)$ and for conventional ASM.

The segmentation result of KPCA-based ASM is compared with the conventional ASM in Tables 2, 3, 4 and 5 for 5 phases of a cardiac cycle (phases 1, 5, 10, 15, 20). The result of KPCA for 4 different values of σ versus conventional ASM is shown for each phase. Tables 2 and 3 show the volume error of epicardium and endocardium, respectively. As it is clear from the tables, the volume error is almost lower for our method than the conventional ASM.

Tables 4 and 5 show the mean and standard deviation of the MAD distance of KPCA and PCA-based ASM for the phases 1, 5, 10, 15 and 20. It can be seen from the tables that overall, our proposed method obtains smaller MAD than the conventional ASM. Besides, the MAD distance is almost lower for endocardium. Increasing the value of σ will increases the MAD distance for both endocardium and epicardium.

Discussion

In this paper, a spatio-temporal statistical shape model of the LV was proposed. Kernel PCA was used to model the nonlinear inter-subject and intra-subject variation of landmarks. The nonlinear model was compared with PCA- and ICA-based 4D models using the standard measures compactness capacity, generalization ability and specificity. The KPCA-based 4D ASM was applied for LV segmentation and evaluated for 5 phases of a cardiac cycle. The results were compared with the conventional ASM.

The high values of the mean of kappa measure and its low value of standard deviation for all local transformations showed the accuracy of the non-rigid registration. As all phases of each dataset were registered to its end-diastolic phase, the lowest value of Kappa measure for global transformation was for the end-systolic phase (phase 9). These reported kappa scores were not the actual measures of registration accuracy. Using the kappa measure, the quality of registration for different phases of a cardiac cycle can be compared with each other. To evaluate the real accuracy of registration, independently placed landmarks are needed.

The compactness of the nonlinear KPCA-based model was controlled by the parameter σ. For high values of σ, the model will be similar to PCA-based model and for low values the compactness curve will tend to the straight line. The compactness capacity of KPCA-based model was generally better than ICA-based model.

For a constants number of modes, the reconstruction error was a little higher for the KPCA-based model than PCA-based and ICA-based model. This occurred due to the error of KPCA-based pre-image reconstruction. Improving the algorithm of reconstruction will decrease this error. The specificity error of KPCA-based model was lower than ICA-based and PCA-based models for almost all values of the parameterσ. In both inter-subject and intra-subject distributions, decreasing the value of the parameterσ will reduce the specificity error.

As it was clear from the Fig. 12 and Tables 2 and 3, the absolute volume error was lower for endocardium than epicardium. As we expected, the average error increased as the value of parameter σ increased. For higher value of σ, the behavior of KPCA-based ASM will be the same as conventional ASM. The volume error was lower for our method than conventional ASM for most of the 5 cardiac phases. Furthermore, the segmentation error for end-systolic phase was more than end-diastolic phase for both methods. The same results were achieved by calculating the MAD distance in Tables 4 and 5. These facts prove the privilege of our proposed method compared with the conventional ASM.

Conclusion

We have presented a 4D statistical model of the left ventricle using cardiac short-axis MR images. This model describes the variation of cardiac anatomy and motion over the cardiac cycle. The extended registration method enables better temporal and spatial alignment of the cardiac dataset. Due to the nonlinear relationship between 3D pseudo-landmarks in each frame, nonlinear PCA was found more appropriate to approximate the LV 4D statistical model.

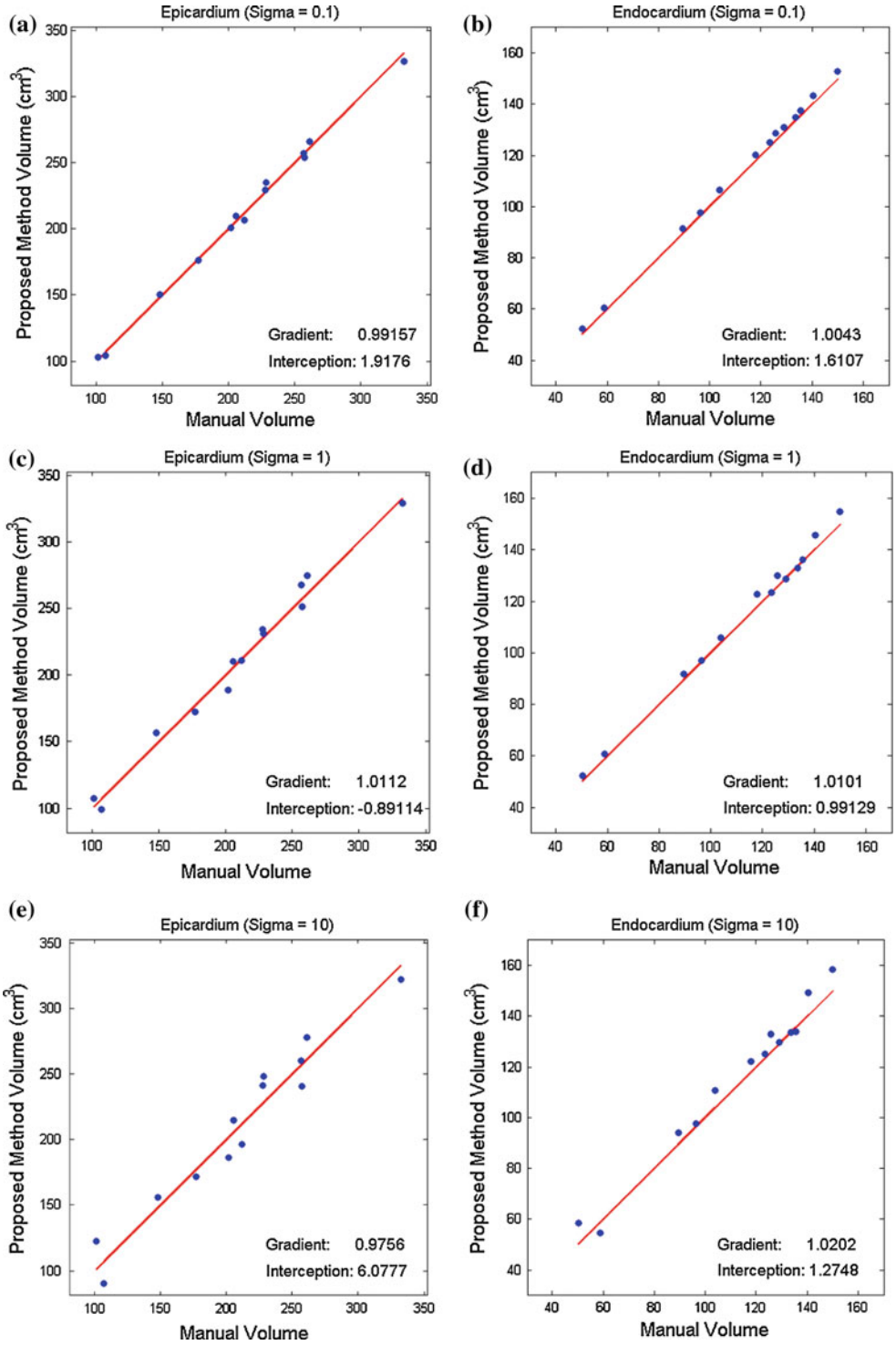

Fig. 12 The regression graph of the KPCA-based ASM (*vertical*) and PCA-based ASM (**i**, **j**) versus manual segmentation (*horizontal*) for the volume inside epicardium (**a**, **c**, **e**, **g**, **i**) and endocardium (**b**, **d**, **f**, **h**, **j**). The model was applied to the end-diastolic phase of a cardiac cycle. The graph is plotted for different value of parameter σ (**a**, **b**, $\sigma = 0.1$; **c**, **d**, $\sigma = 1$; **e**, **f**, $\sigma = 10$; **g**, **h**, $\sigma = 100$). The segmentation result is more precise for endocardium

Nonlinear property of KPCA will strengthen the ability of SSM in image segmentation. This fact was demonstrated in this paper by applying 4D KPCA-based ASM to all phases of a cardiac cycle. We are now continuing the research toward segmenting the LV using 4D KPCA-based ASM or AAM. Besides, the AAM models will be applied in patients that

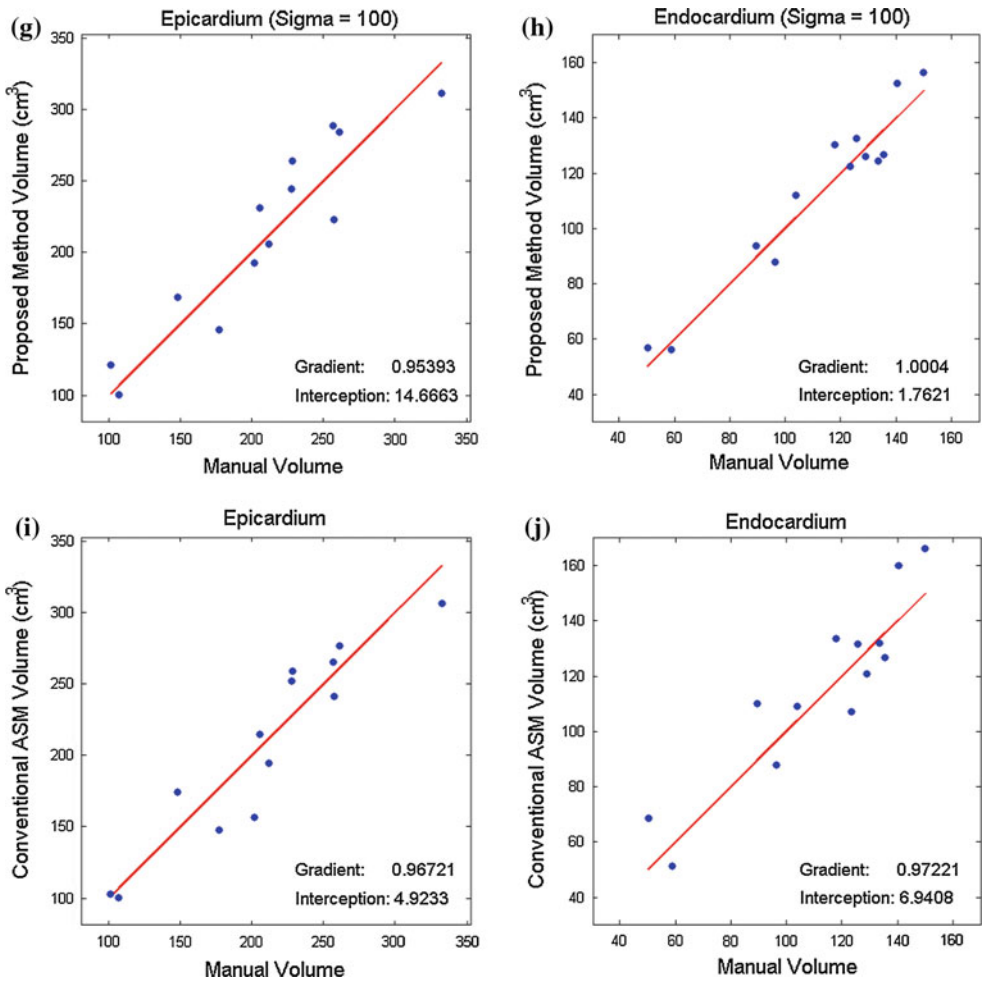

Fig. 12 continued

Table 2 Segmentation results of epicardium for the proposed method compared with the PCA-based ASM

	KPCA-based ASM ($\sigma = 0.1$)	KPCA-based ASM ($\sigma = 1$)	KPCA-based ASM ($\sigma = 10$)	KPCA-based ASM ($\sigma = 100$)	PCA-based ASM
Phase 1	4.49 ± 3.65	5.76 ± 4.18	11.32 ± 6.42	15.57 ± 3.12	16.95 ± 6.28
Phase 5	7.91 ± 4.12	9.83 ± 4.96	15.81 ± 4.45	16.81 ± 7.74	17.64 ± 4.55
Phase 10	10.08 ± 5.93	12.19 ± 4.25	15.66 ± 5.76	20.76 ± 5.26	20.01 ± 4.30
Phase 15	5.67 ± 4.32	8.45 ± 3.35	13.43 ± 6.11	18.44 ± 4.83	18.37 ± 7.02
Phase 20	3.21 ± 3.74	6.91 ± 4.84	13.25 ± 6.27	21.76 ± 6.05	19.72 ± 6.21

All values are mean $\pm$ SD absolute volume errors in cm^3. These methods were applied to 5 phases of a cardiac cycle. The KPCA-based method was applied for 4 different values of parameter σ

have pathologies in myocardium. For LV segmentation and quantification of the LV volumes, the position of the mitral valve plane is needed. For a realistic 4D LV model, this information should be integrated. In addition, the model can be constructed for other chambers of the heart such as atria or right ventricle.

A fully automated system as described in this paper can potentially produce uniform data with minimum inter-observer variability. Currently hand tracing of the ventricular contour is the norm in most cardiac MRI studies. But that approach is prone to inter-observer variability. For instance whether or not to include the left ventricular trabeculations or the papillary muscles may differ from one operator to another or among different institutions. Similarly the problem of partial inclusion of the left atrium, as the mitral valve plane moves inward during systole, is interpreted differently by

Table 3 Segmentation results of endocardium for the proposed method compared with the PCA-based ASM

	KPCA-based ASM ($\sigma = 0.1$)	KPCA-based ASM ($\sigma = 1$)	KPCA-based ASM ($\sigma = 10$)	KPCA-based ASM ($\sigma = 100$)	PCA-based ASM
Phase 1	1.81 ± 1.64	3.31 ± 2.46	6.27 ± 4.53	6.02 ± 7.50	9.62 ± 11.37
Phase 5	3.45 ± 2.03	2.73 ± 1.69	4.82 ± 3.06	5.52 ± 9.04	14.36 ± 9.91
Phase 10	4.37 ± 1.75	4.95 ± 1.45	6.60 ± 5.44	7.39 ± 5.83	13.92 ± 9.04
Phase 15	1.54 ± 1.34	3.42 ± 2.75	4.16 ± 3.37	5.63 ± 10.25	10.48 ± 7.52
Phase 20	2.08 ± 2.15	2.26 ± 3.80	4.43 ± 5.54	6.87 ± 10.06	11.73 ± 11.98

All values are mean $\pm$ SD absolute volume errors in cm^3. These methods were applied to the 5 phases of a cardiac cycle. The KPCA-based method was applied for 4 different values of parameter σ

Table 4 Comparison of the MAD distance between the KPCA-based and conventional ASM for the epicardium

	KPCA-based ASM ($\sigma = 0.1$)	KPCA-based ASM ($\sigma = 1$)	KPCA-based ASM ($\sigma = 10$)	KPCA-based ASM ($\sigma = 100$)	PCA-based ASM
Phase 1	2.53 ± 0.30	2.75 ± 0.85	2.96 ± 1.85	3.16 ± 1.93	4.25 ± 1.61
Phase 5	1.72 ± 0.93	3.18 ± 1.98	3.39 ± 1.56	5.15 ± 2.06	4.88 ± 1.52
Phase 10	3.69 ± 0.57	3.91 ± 1.91	4.72 ± 0.41	6.02 ± 1.84	5.40 ± 2.53
Phase 15	1.35 ± 0.41	2.16 ± 1.44	3.52 ± 1.41	4.59 ± 2.23	5.13 ± 2.21
Phase 20	2.16 ± 013	2.45 ± 1.16	2.80 ± 1.08	3.28 ± 1.99	3.14 ± 1.83

All values are mean $\pm$ SD. These methods were applied to 5 phases of a cardiac cycle. The KPCA-based method was applied for 4 different values of parameter σ

Table 5 Comparison of the MAD distance between the KPCA-based and conventional ASM for the endocardium

	KPCA-based ASM ($\sigma = 0.1$)	KPCA-based ASM ($\sigma = 1$)	KPCA-based ASM ($\sigma = 10$)	KPCA-based ASM ($\sigma = 100$)	PCA-based ASM
Phase 1	2.05 ± 1.28	2.53 ± 1.58	2.41 ± 1.26	2.70 ± 1.32	3.66 ± 1.46
Phase 5	1.34 ± 0.53	1.56 ± 1.13	2.74 ± 1.13	3.26 ± 1.95	3.58 ± 2.05
Phase 10	2.39 ± 0.64	2.65 ± 1.75	2.96 ± 0.97	3.48 ± 1.47	4.29 ± 1.84
Phase 15	1.20 ± 0.75	1.78 ± 1.51	2.02 ± 1.46	3.18 ± 1.86	3.85 ± 2.34
Phase 20	1.28 ± 0.43	1.35 ± 0.97	1.49 ± 0.67	2.40 ± 0.95	2.95 ± 1.46

All values are mean $\pm$ SD. These methods were applied to 5 phases of a cardiac cycle. The KPCA-based method was applied for 4 different values of parameter σ

different human operators. Once validated, it could enhance the clinical utility of MRI in the assessment of cardiac function in patient studies.

Conflict of interest None.

References

1. American Heart Association (2010) 2010 Heart and Stroke Statistical Update. [Online]. Available: http://www.americanheart.org
2. Frangi AF, Niessen WJ, Viergever MA (2001) Three-dimensional modeling for functional analysis of cardiac images: a review. IEEE Trans Medical Imaging 20(1):2–25
3. Jolly MP, Xue H, Grady L, Gühring J (2009) Combining registration and minimum surfaces for the segmentation of the left ventricle in cardiac cine MR images. In: Proceedings MICCAI, LNCS 5762, pp 910–918
4. Cousty J, Najman L, Couprie M, Clément-Guinaudeau S, Goissen T, Garot J (2010) Segmentation of 4D cardiac MRI: automated method based on spatio-temporal watershed cuts. J Image Vis Comput 28(8):1229–1243
5. Schaerer C, Casta C, Pousin J, Clarysse P (2010) A dynamic elastic model for segmentation and tracking of the heart in MR image sequences. Medical Image Anal 14(6):738–749
6. Grande LC, Ferrero GVS, de la Higuera PC, Calvar JASR, Orodea AR, Fernández MM, López CA (2011) Unsupervised 4D myocardium segmentation with a Markov random field based deformable model. Medical Image Anal 15(3):283–301
7. Zhuang X, Rhode KS, Razavi RS, Hawkes DJ, Ourselin S (2010) A registration-based propagation framework for automatic whole heart segmentation of cardiac MRI. IEEE Trans Medical Imaging 29(9):1612–1625
8. Petitjean C, Dacher JN (2011) A review of segmentation methods in short axis cardiac MR images. Medical Image Anal 15(2):169–184
9. Heimann T, Meinzer HP (2009) Statistical shape models for 3D medical image segmentation: a review. Medical Image Anal 13(4):543–563

10. Rueckert D, Frangi AF, Schnabel JA (2003) Automatic construction of 3D statistical deformation models of the brain using nonrigid registration. IEEE Trans Medical Imaging 22(8):1014–1025
11. Lorenzo-Valdes M, Sanchez-Ortiz GI, Elkington A, Mohiaddin R, Rueckert D (2004) Segmentation of 4D cardiac MR images using a probabilistic atlas and the EM algorithm. Medical Image Anal 8(3):255–265
12. Pilgram R, Schubert R, Fritscher KD, Zwick RH, Schocke MF, Trieb T, Pachinger O (2006) Shape discrimination of healthy and diseased cardiac ventricles using medial representation. Int J CARS 1(1):33–38
13. Cootes TF, Taylor CJ, Cooper DH, Graham J (1995) Active shape models: their training and application. Comput Vis Image Understand 61(1):38–59
14. Frangi AF, Rueckert D, Schnabel JA, Niessen WJ (2002) Automatic construction of multiple-object three-dimensional statistical shape models: application to cardiac modeling. IEEE Trans Medical Imaging 21(9):1151–1164
15. Lotjonen J, Kivisto S, Koikkalainen J, Smutek D, Lauerma K (2004) Statistical shape model of atria, ventricles and epicardium from short- and long-axis MR images. Medical Image Anal 8(3):371–386
16. Ordas S, Oubel E, Leta R, Carreras F, Frangi AF (2007) A statistical shape model of the heart and its application to model-based segmentation. In: Proceedings of SPIE medical imaging, vol 6511
17. Perperidis D, Mohiaddin R, Rueckert D (2005) Construction of a 4D statistical atlas of the cardiac anatomy and its use in classification. In: Proceedings of MICCAI, LNCS 3750, pp 402–405
18. Stegmann MB, Pedersen D (2005) Bi-temporal 3D active appearance models with applications to unsupervised ejection fraction estimation. In: Proceedings of SPIE medical imaging, vol 5747, pp 336–350
19. Zhang H, Wahle A, Johnson RK, Scholz TD, Sonka M (2010) 4D cardiac MR image analysis: left and right ventricular morphology and function. IEEE Trans Medical Imaging 29(2):350–364
20. Zhu Y, Papademetris X, Sinusas AJ, Duncan JS (2010) Segmentation of the left ventricle from cardiac MR images using a subject-specific dynamical model. IEEE Trans Medical Imaging 29(3):669–687
21. O'Brien SP, Ghita O, Whelan PF (2011) A novel model-based 3D+time left ventricular segmentation technique. IEEE Trans Medical Imaging 30(2):461–474
22. Suinesiaputra A, Frangi AF, Kaandorp TAM, Lamb HJ, Bax JJ, Reiber JHC, Lelieveldt BPF (2009) Automated detection of regional wall motion abnormalities based on a statistical model applied to multislice short-axis cardiac MR images. IEEE Trans Medical Imaging 28(4):595–607
23. Twining CJ, Taylor CJ (2001) Kernel principal component analysis and the construction of non-linear active shape models. In: Proceedings of British machine vision conference, vol 1, pp 23–32
24. Uzumcu M, Frangi AF, Reiber JHC, Lelieveldt BPF (2003) Independent component analysis in statistical shape models. In: Proceedings of SPIE medical imaging, vol 5032, pp 375–383
25. Koikkalainen J, Lotjonen J (2004) Image segmentation with the combination of PCA- and ICA-based modes of shape variation. In: Proceedings of IEEE international symposium on biomedical imaging: from Nano to Macro, vol 1, pp 149–152
26. Hilger KB, Larsen R, Wrobel MC (2003) Growth modeling of human mandibles using non-euclidean metrics. Medical Image Anal 7(4):425–433
27. Larsen R, Hilger KB (2003) Statistical shape analysis using non-Euclidean metrics. Medical Image Anal 7(4):417–423
28. Dambreville S, Rathi Y, Tannenbaum A (2008) A framework for image segmentation using shape models and kernel space shape priors. IEEE Trans Pattern Anal Mach Intell 30(8):1385–1399
29. Rathi Y, Dambreville S, Tannenbaum A (2006) Comparative analysis of kernel methods for statistical shape learning. In: Proceedings of 2nd international workshop computer vision approaches to medical image analysis, vol 2
30. Cremers D, Kohlberger T, Schnorr C (2003) Shape statistics in kernel space for variational image segmentation. Pattern Recogn 36:1929–1943
31. Andreopoulos A, Tsotsos JK (2008) Efficient and generalizable statistical models of shape and appearance for analysis of cardiac MRI. Medical Image Anal 12(3):335–357
32. Herman GT, Zheng J, Bucholtz CA (1992) Shape-based interpolation. IEEE Comput Graph Appl, 69–79
33. Raya S, Udupa J (1990) Shape-based interpolation of multidimensional objects. IEEE Trans Medical Imaging 9(1):33–42
34. Newman T, Yi H (2006) A survey of the marching cubes algorithm. Comput Graph 30(5):854–879
35. Knapp M (2002) Mesh decimation using VTK, Technical report, Vienna University of Technology
36. Goodall C (1991) Procrustes methods in the statistical analysis of shape. J R Stat Soc 53(2):285–339
37. Cootes TF (2004) Statistical models of appearance for computer vision, Technical Report, University of Manchester
38. Davies R, Twining C, Taylor C (2008) Statistical models of shape: optimization and evaluation. 1st edn. Springer, London
39. Twining CJ, Taylor CJ (2003) The use of kernel principal component analysis to model data distribution. Pattern Recogn 36:217–227
40. Mika S, Scholkopf B, Smola A, Muller K, Scholz M, Ratsch G (1998) Kernel PCA and denoising in feature spaces. Adv Neural Inf Process Syst 11
41. Kwok , Tsang I (2004) The pre-image problem in kernel methods. IEEE Trans Neural Netw 15(6):1517–1525
42. Rathi Y, Dambreville S, Tannenbaum A (2006) Statistical shape analysis using kernel PCA. In: Proceedings of SPIE medical imaging, vol 6064, pp 425–432
43. Department of Computer Science and Engineering, Centre for Vision Research, York University. [Online]. Available: http://www.cse.yorku.ca/~mridataset/
44. Schnabel A, Rueckert D, Quist M, Blackall JM, Castellano Smith AD, Hartkens T, Penney GP, Hall WA, Liu H, Truwit CL, Gerritsen FA, Hill DLG, Hawkes DJ (2001) A generic framework for non-rigid registration based on non-uniform multi-level free-form deformations. In: Proceedings of MICCAI, LNCS 2208, pp 573–581
45. Avila Lisa S, Barre S, Blue R, Cole D, Geveci B, Hoffman WA, King B, Law CC, Martin KM, Schroeder WJ, Squillacote AH, The VTK User's Guide (2011) Kitware, 11th edn., New York
46. Franc V, Hlavac V (2004) Statistical pattern recognition toolbox for MATLAB, Technical Report, Czech Technical University Prague, June 2004
47. Leiner B, Jimena O, Boris ER, Fernando A, Enrique V (2012) Segmentation of 4D cardiac computed tomography images using active shape models. In: Proceedings of SPIE medical imaging, vol 8436
48. Kroon D-J. Active shape model (ASM) and active appearance model (AAM). Available: http://www.mathworks.com/matlabcentral/fileexchange/